Research Article | Vol. 28, No. 20 / 28 September 2020 / Optics Express 29513
Optics EXPRESS

Giant polarization anisotropic optical response from anodic aluminum oxide templates embedded with plasmonic metamaterials

YUYI FENG,[1] PAUL LEIDERER,[2] RUIZHE ZHAO,[1] XIAOFEI XIAO,[3] VINCENZO GIANNINI,[4] STEFAN A. MAIER,[3,5] CLAYTON A. NEMITZ,[6] ZEMENG LIN,[1] NING DING,[1] GUOGUO KANG,[1] DEWEN CHENG,[1] LUKAS SCHMIDT-MENDE,[2] LINGLING HUANG,[1,7] AND YONGTIAN WANG[1,8]

[1]*School of Optics and Photonics, Beijing Institute of Technology, Beijing, 100081, China*
[2]*Department of Physics, University of Konstanz, Konstanz, 78457, Germany*
[3]*Department of Physics, Imperial College London, London, SW7 2AZ, United Kingdom*
[4]*Instituto de Estructura de la Materia (IEM), Consejo Superior de Investigaciones Científicas (CSIC), Serrano 121, Madrid, 28006, Spain*
[5]*Chair in Hybrid Nanosystems, Nanoinstitut München, Faculty of Physics, Ludwig-Maximilians-Universität München, München, 80539, Germany*
[6]*Department of Physics and Astronomy, University of North Carolina, Chapel Hill, North Carolina 27516, USA*
[7]*huanglingling@bit.edu.cn*
[8]*wyt@bit.edu.cn*

Abstract: Plasmonic metamaterials enable extraordinary manipulation of key constitutive properties of light at a subwavelength scale and thus have attracted significant interest. Here, we report a simple and convenient nanofabrication method for a novel meta-device by glancing deposition of gold into anodic aluminum oxide templates on glass substrates. A methodology with the assistance of ellipsometric measurements to examine the anisotropy and optical activity properties is presented. A tunable polarization conversion in both transmission and reflection is demonstrated. Specifically, giant broadband circular dichroism for reflection at visible wavelengths is experimentally realized by oblique incidence, due to the extrinsic chirality resulting from the mutual orientation of the metamaterials and the incident beam. This work paves the way for practical applications for large-area, low-cost polarization modulators, polarization imaging, displays, and bio-sensing.

1. Introduction

Metamaterials consisting of subwavelength metallic/dielectric nanostructures have received increasing attention due to their unprecedented ability to manipulate light [1]. They have shown great promise for a wide variety of practical applications, such as optical communication [2,3], bio-sensing [4,5], imaging [6,7], data storage [8,9], displays [10–13], invisibility cloaking [14,15], and photovoltaics [16,17]. An important feature of metamaterials is the strong light-matter interaction and the possibility of introducing strong optical anisotropy (i.e., a phenomenon that is observed when the speed of light in a medium depends on the polarization plane of the incident electromagnetic wave), which is sensitive to the angle of incidence and polarization state of the incoming light, making them attractive candidates for polarization optics [18–23]. Meanwhile, optical activity, that is, the ability to rotate the polarization state of light, is a fascinating physical phenomenon. In particular, circular dichroism (CD), which originates from the asymmetric interaction of a system to left and right circularly polarized light, is of great importance for chiral

#403437 https://doi.org/10.1364/OE.403437
Journal © 2020 Received 24 Jul 2020; revised 25 Aug 2020; accepted 25 Aug 2020; published 18 Sep 2020

Optics EXPRESS

biosensing [24–27], disease diagnosis [28], super-resolution imaging [29], nanorobotics [30], and drug development [31]. However, CD has quite a weak optical signature in natural materials. To overcome this challenge, the traditional way is to develop plasmonic nanostructures with a chiral shape such as twisters [32,33], gammadions [34], and helices [35] with subwavelength resolutions, in order to significantly boost the CD signals. Using the tunable mechanism of phase change materials under external stimuli is one of the important ways to achieve dynamic chirality [36]. However, for those well-defined nanostructures, they are usually demanding e-beam lithography (EBL) and focusing ion beam (FIB), and laser precision engineering such as microlens arrays (MLA) lithography and femtosecond two-photon polymerization (2PP) lithography [37,38], which are costly and time-consuming, limiting the practical applications especially when large area or high throughput are needed. Therefore, novel plasmonic metamaterials with a high CD response in the visible light and a fast and scalable fabrication method remain urgently necessary.

Recently, alternative fabrication methods have been developed. For instance, an aligned lithography technique has been used to make a twisted stack of achiral structures that exhibit optical activity [39]. However, lithography facilities with high-resolution alignment and delicate operations are required. Another example is a polystyrene sphere template assisted glancing angle deposition method that has been developed to fabricate 3D nanocrescent arrays [40]. However, the process is complicated and the circular dichroism (CD) signals are relatively low. Anodic aluminum oxide (AAO) templates have opened a new route of producing large-area metamaterials in a simple and efficient way, with the advantages of excellent chemical, thermal and mechanical stabilities. Moreover, the geometries of the AAOs can easily be varied in a wide range by changing the anodization conditions, and the nanopores can easily be filled with various metallic and dielectric materials. However, most previous work on the fabrication of the AAO membranes was performed using thick (~ mm) Al foils, followed by etching away the remaining Al, leaving a fragile, unsupported AAO membrane poorly suited for optical metamaterial device fabrication [41–45]. Therefore, it is essential to develop a method for the fabrication of AAO-embedded metamaterials with high CD signals directly on a glass or quartz substrate.

Here, we report an industrially applicable nanofabrication method for producing AAO-embedded Au metamaterials with strong optical anisotropy in visible light on glass substrates, through a combination of a low-cost anodization process of AAO membranes and a rapid and efficient glancing angle thermal deposition. Unlike the typical chiral media, we present experimental and numerical results showing that a non-chiral sample can produce giant CD at oblique incident angles. The largest CD of 0.75 is obtained at a wavelength of 430 nm with an incident angle of 70°. To demonstrate the polarization conversion effect, we also show that the output polarization ellipse can be finely tuned by varying the angle of incident linearly polarized light. This method could be exploited for developing novel high efficiency polarization modulators, polarization imaging systems, and biosensors.

2. Results and discussion

A schematic diagram of the nanofabrication method using oblique angle deposition, which is also known as glancing angle deposition (GLAD), is shown in Fig. 1. This method offers the opportunity to create complex nanoarchitectures over large areas in a fast manner. The Au is thermally deposited into transparent substrate-supported anodic aluminum oxide (AAO) templates, with a glancing angle of $\alpha = 30°$, while rotating the substrate at 6 rpm for durations ranging from 300 s to 400 s, as depicted in Figs. 1(a) and 1(b). The deposition rate of Au is 0.1 nm/s. Specifically, a portion of the Au atoms penetrate into the AAO nanohole and fall onto the inside walls, acting as seeds on to which the subsequent incoming atoms nucleate and grow in an inverted conical manner, owing to the amplified shadowing effect. For the fabrication of the AAO template, an Al film 200 nm thick is deposited on a substrate by magnetron sputtering. The substrate is comprised of a thick ITO-coated glass slide with a 5 nm thick adhesive layer of Ti

Optics EXPRESS

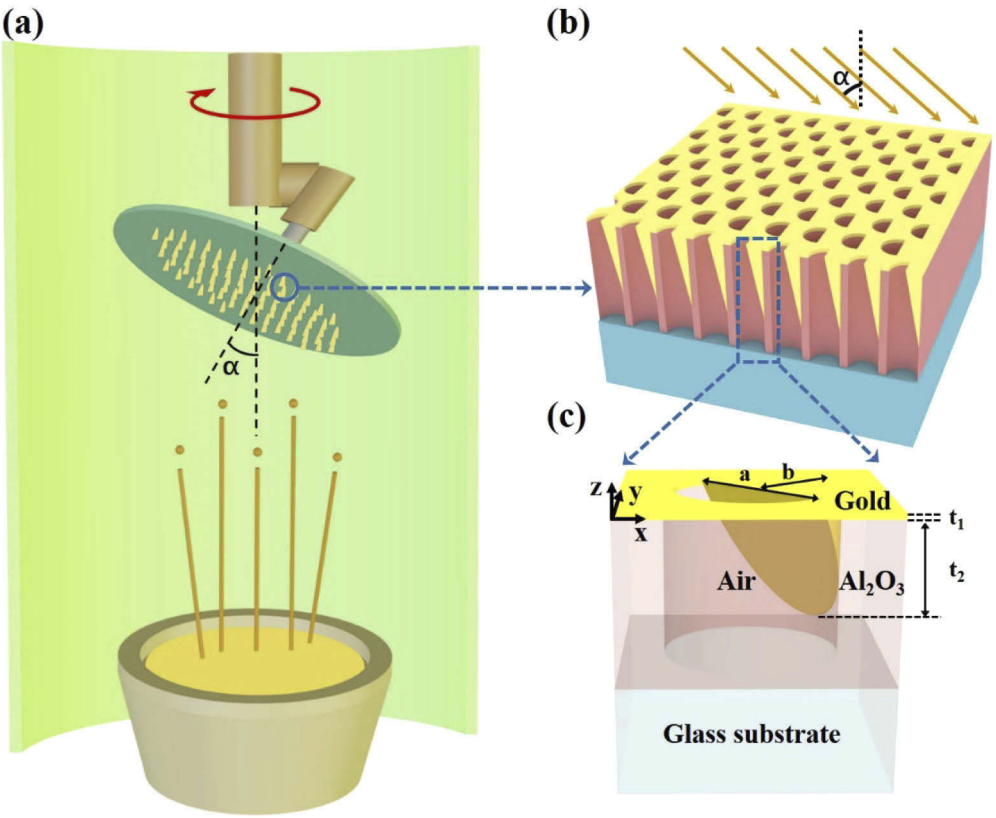

Fig. 1. Fabrication scheme. (a) Schematic illustration of glancing angle deposition by thermal evaporation. The angle between the normal of the substrate and the incoming flux is α. During the deposition, the substrates spins along the direction of the red arrow. (b) Schematic side view of a uniform array of anodic aluminum oxide (AAO) templates embedded gold irregular nanostructures on glass substrates. (c) Schematic side view of a single unit cell. The cylindrical Al_2O_3 nanohole is grown on a glass substrate, covered and half filled with gold. The diameter, height and lattice constant of the nanohole are 80 nm, 300 nm and 113 nm, respectively.

and a 2 nm thick Au layer. The highly uniform, large-area, quasi-hexagonal AAO template was produced by anodization in oxalic acid at 40 V. A thorough description of AAO can be found in our previous work [46]. The resulting nano-inverted conical Au assembly is strongly anisotropic, as shown in the scanning electron microscopic images in Figs. 2(a) and 2(b), which show a top and a cross-sectional view, respectively. Based on the SEM images, a schematic geometry of a single unit cell is proposed in Fig. 1(c), which consists of a cylindrical aluminum oxide nanohole, a superimposed coaxial gold nanoaperture, and an inverted gold nanocone situated inside. The average diameter, height, and spacing of the AAO pores are estimated to be 80 nm, 300 nm, and 133 nm, respectively (by ImageJ analysis software). The thickness of the gold nanoaperture and the height of the inverted gold nanocone in the AAO pore are denoted by t_1 and t_2. The long axis and short axis of the top of the inverted gold nanocone are defined as a and b. Unless otherwise stated, $t_1 = 33 \pm 5$ nm, $t_2 = 178 \pm 10$ nm, $a = 70 \pm 10$ nm, and $b = 42 \pm 10$ nm in all calculations.

We investigated the spectral response of the meta-device at different wavelengths ranging from 400 nm to 820 nm using a reflection-transmission ellipsometer (J. A. Woollam VASE), shown in Fig. 2(c). The transmission and reflection spectra as well as ellipsometric parameters

Optics EXPRESS

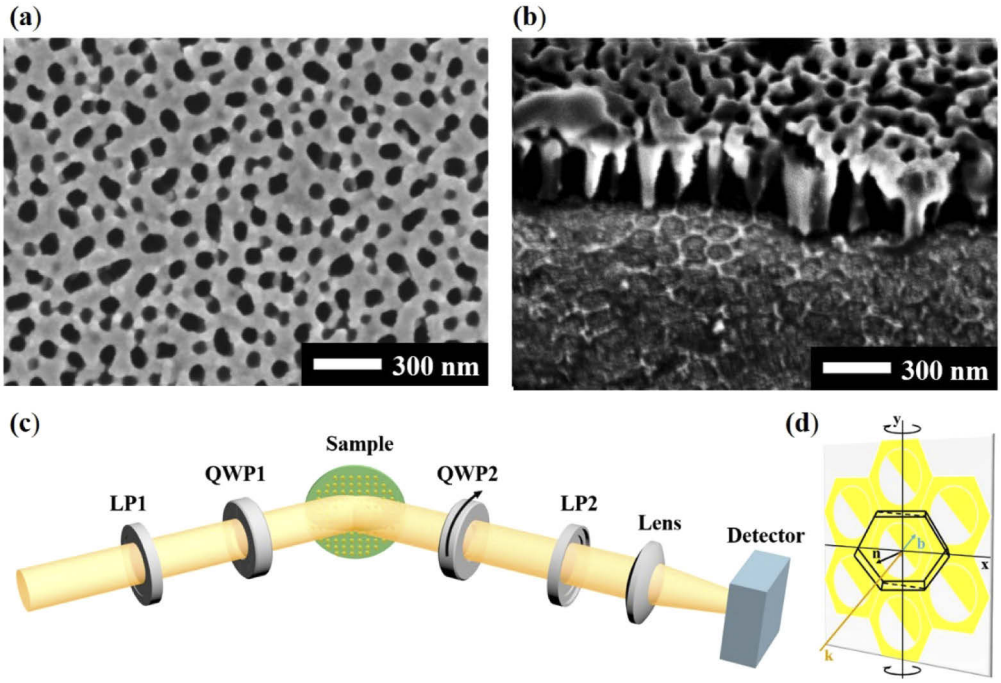

Fig. 2. Metamaterials and optical setup. (a) Scanning electron microscopy (SEM) top view of the fabricated metamaterials. (b) SEM side view of the fabricated metamaterials. The stage angle is 54°. (c) Schematic illustration of the optical measurement setup. The linear polarizer (LP1) and quarter-wave plate (QWP1) are used to produce any desired state of polarization of the incident beam. The output beam can be subsequently analyzed by means of an analyzer consisting of a rotating quarter-wave plate (QWP2) and a linear polarizer (LP2). (d) Schematic illustration of the top view of the sample at oblique incident light. Note that k is the wave vector of the incident light, n is the sample normal, and b is the direction of the symmetry axis (i.e., the direction of the short axis of the nanocone).

($\Psi, \Psi_{ps}, \Psi_{sp}$) and ($\Delta, \Delta_{ps}, \Delta_{sp}$) were recorded for angles of incidence from 20° to 70° in 5° increments in the 400 - 820 nm wavelength range every 5 nm. Figure 3(a) illustrates the measured transmittance spectra of the meta-device. As seen in Fig. 3(a), for wavelengths ranging from 400 nm to 820 nm, there is one peak at 500 nm for both p- and s- polarized excitations, originating from the localized plasmonic resonance. We also observe that at a small angle of incidence, for instance 20°, the p- and s- curves are almost the same, indicating nearly no anisotropicity of the system. However, as the angle of incidence (AOI) increases, the s-polarized spectrum tends to be flatter than the p-polarized spectrum, while the resonance peak of p polarization is blue shifted, indicating the occurrence of anisotropy of the system at larger AOI. To gain further insight, we plot the 2D maps of the measured transmittance as a function of wavelength and angle of incidence under p- and s- excitation, respectively [Figs. 3(d) and 3(g)]. We observe that at AOI over 50°, the anisotropy becomes pronounced, especially at a wavelength of 500 nm. As a next step, we investigate the reflective response of the meta-device. Figures 3(b), 3(e) and 3(h) show the measured reflectivity. We observe that at small AOI (20° - 30°), there is a broad bandwidth reflection at wavelengths ranging from 500 nm to 820 nm for both p- and s- excitations. However, with an increased AOI (40° - 60°), for s-polarized excitation, the feature of the spectra is dominated by a relatively sharp peak. More interestingly, the peak blue shifts by 50 nm from 500 nm to 450 nm. In contrast, the p- polarized spectra are much flatter. The

Optics EXPRESS

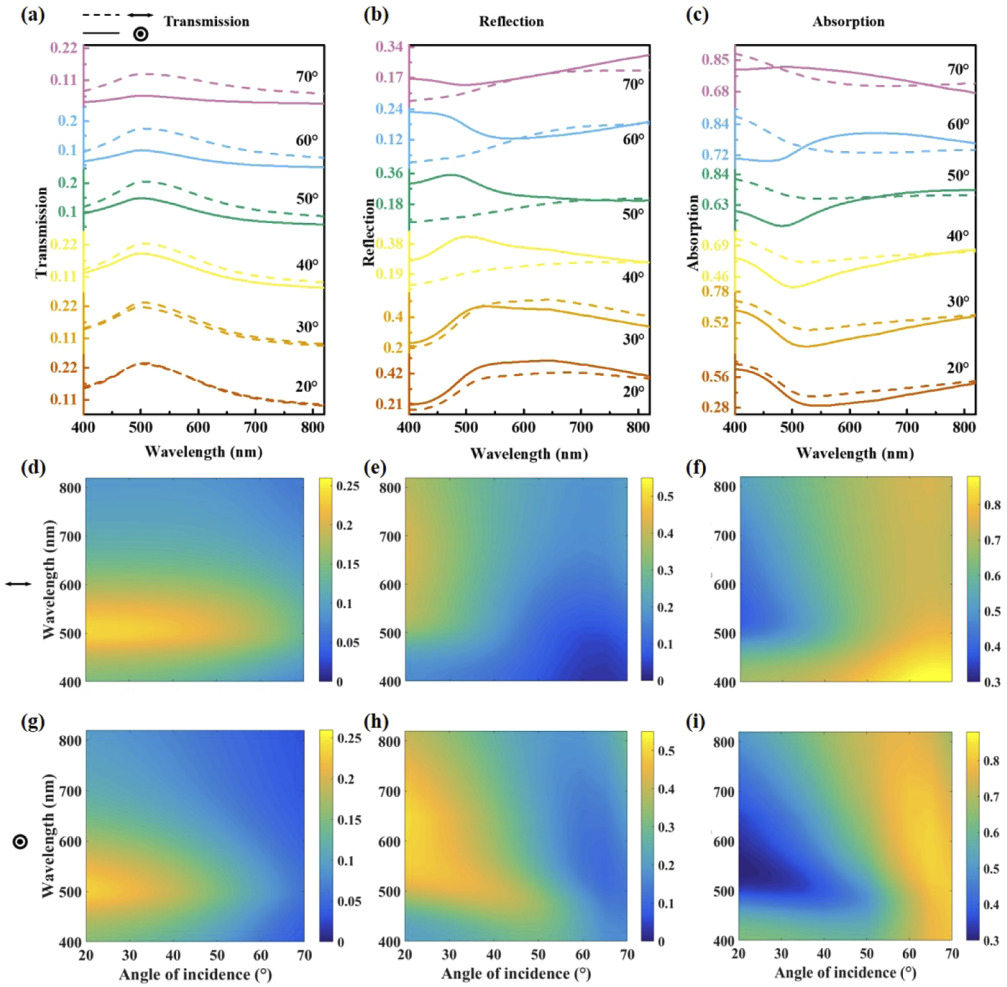

Fig. 3. Optical response under linearly polarized excitation. (a-c) Transmission, reflection and absorption spectra of the sample at different angles of incidence of p- and s- polarized light. (d-f) Contour mappings of p-polarized light, corresponding to a-c. (g-i) Contour mappings of s-polarized light, corresponding to a-c.

difference in the behaviors of p- and s- polarized reflectance indicates strong anisotropy at large AOI. Additionally, at even larger AOI (i.e., 70°), the deviation between p- and s- polarized spectra is mainly limited to short wavelengths between 400 and 500 nm, indicating an anisotropy within a narrow bandwidth. To study the meta-device absorption behavior, we obtained the absorption (A) by using A=1-T-R, where T is transmission and R is reflection, as shown in Figs. 3(c), 3(f) and 3(i). It is seen that in the range of 400 nm to 820 nm, the anisotropic behavior, which is dependent on the incident angle, is similar to that of the reflection case.

The origin of the effect in the meta-device may be explained by a simplified model of a period, which contains a single irregular nanocone [Fig. 1(c)]. The nanocone array is in a hexagonal arrangement and possess C1-symmetry, with respect to the main diagonal of the XY-plane. At small angles of incidence (i.e., near normal incidence), the p-polarized (i.e., x-polarized) and s-polarized (i.e., y-polarized) light excite the gold nanostructure almost in a symmetric manner, resulting in almost isotropic optical responses. At large AOI, the oblique incidence further breaks

Optics EXPRESS

the symmetry, leading to different plasmonic modes, resulting in pronounced anisotropic optical responses. This effect is further verified by the finite difference time domain simulations with a periodic boundary condition, which can be found in the Appendix Note A1, Note A2, and Fig. 7 and Figs. 8(a)–8(p).

To evaluate the optical activity of the meta-device, we first measured the ellipsometric parameters ($\Psi, \Psi_{ps}, \Psi_{sp}$), the amplitude ratio between the linear polarization components, and ($\Delta, \Delta_{ps}, \Delta_{sp}$), the phase difference between the linear polarization components, at incident angles from 20° to 70°. We then obtained the full reflection and transmission coefficients, that is, R_{pp}, R_{ps}, R_{sp}, and R_{ss}, of the complex Jones matrix R, and T_{pp}, T_{ps}, T_{sp}, and T_{ss}, of the complex Jones matrix T, for linearly polarized light. The detailed derivation can be seen in the Appendix (Note A3). The results of the calculated co-polarized and cross-polarized reflection/transmission amplitude spectra in comparison to the experimental reflection intensity spectra at incident angle of 60°are presented in the Appendix Fig. 9. We found that the co-polarized components mainly contribute to the measured reflection/transmission spectra. Interestingly, although the cross-polarized components of $|r_{ps}|$ and $|r_{sp}|$ are relatively small, they differ greatly from each other, with a maximum difference of 89% at 440 nm, normalized by their sum.

Then, we obtain the reflection matrix for circularly polarized light by a change of the base vectors from linear to circular states by the following formula [47]

$$\begin{pmatrix} R_{rr} & R_{rl} \\ R_{lr} & R_{ll} \end{pmatrix} = \frac{1}{2}\begin{pmatrix} R_{pp} - R_{ss} + i(R_{ps} + R_{sp}) & R_{pp} + R_{ss} - i(R_{ps} - R_{sp}) \\ R_{pp} + R_{ss} + i(R_{ps} - R_{sp}) & R_{pp} - R_{ss} - i(R_{ps} + R_{sp}) \end{pmatrix}. \quad (1)$$

Meanwhile, the T matrix for circularly polarized light in the transmittance configuration is written as [48]

$$\begin{pmatrix} T_{rr} & T_{rl} \\ T_{lr} & T_{ll} \end{pmatrix} = \frac{1}{2}\begin{pmatrix} T_{pp} + T_{ss} + i(T_{ps} - T_{sp}) & T_{pp} - T_{ss} - i(T_{ps} + T_{sp}) \\ T_{pp} - T_{ss} + i(T_{ps} + T_{sp}) & T_{pp} + T_{ss} - i(T_{ps} - T_{sp}) \end{pmatrix}. \quad (2)$$

Where r and l refer to right-handed circular polarization (RCP) and left-handed circular polarization (LCP), respectively. Here RCP is defined as a clockwise rotation of the electric field vector at a fixed point when looking into the beam. Note that the CD signal is defined as CD = $(R_{RCP} - R_{LCP})/(R_{RCP} + R_{LCP})$, that is, the difference between the intensity of the reflection (or transmission) of right- and left-handed circularly polarized light, normalized by their sum. Consequently, the transmittance and reflectance under circularly polarized excitation are obtained, as shown in Fig. 4. An example of the calculated co- and cross-circularly polarized spectra at AOI = 60° is shown in the Appendix Fig. 10.

In the case of reflectance [Figs. 4(b), 4(e), and 4(h)], we observe that at small AOI (20°- 40°), there is a broad bandwidth reflection in the 500 - 820 nm range for both left- and right-handed light excitations. Moreover, the differentiation between LCP and RCP is very small in the entire range of wavelength measured, implying a nearly negligible CD signal at small AOI (20°- 40°) in the 400 - 820 nm range. In contrast, as the AOI further increases (50°-70°), the differentiation between LCP and RCP is remarkable, indicating the occurrence of strong CD signals, as presented in Figs. 5(b) and 5(e). For example, at an incident angle of 60°, we observe a significant CD in a broad wavelength range from 400 nm to 820 nm, with a maximum value of 0.25 at 520 nm. Furthermore, the numerical results in the Appendix ew. 10d reveal that the output co-circular polarization states mainly contribute to the CD signal. It is important to note that at an incident angle of 70°, the differentiation between LCP and RCP is only focused on a narrow bandwidth at short wavelengths, resulting in a CD value that exceeds 0.5 from 400 nm to 435 nm with a maximum value of 0.7 attained at 430 nm. These CD signals are comparable to or even surpass the plasmonic optical activity in the visible range in recent studies [29,49–51].

Optics EXPRESS

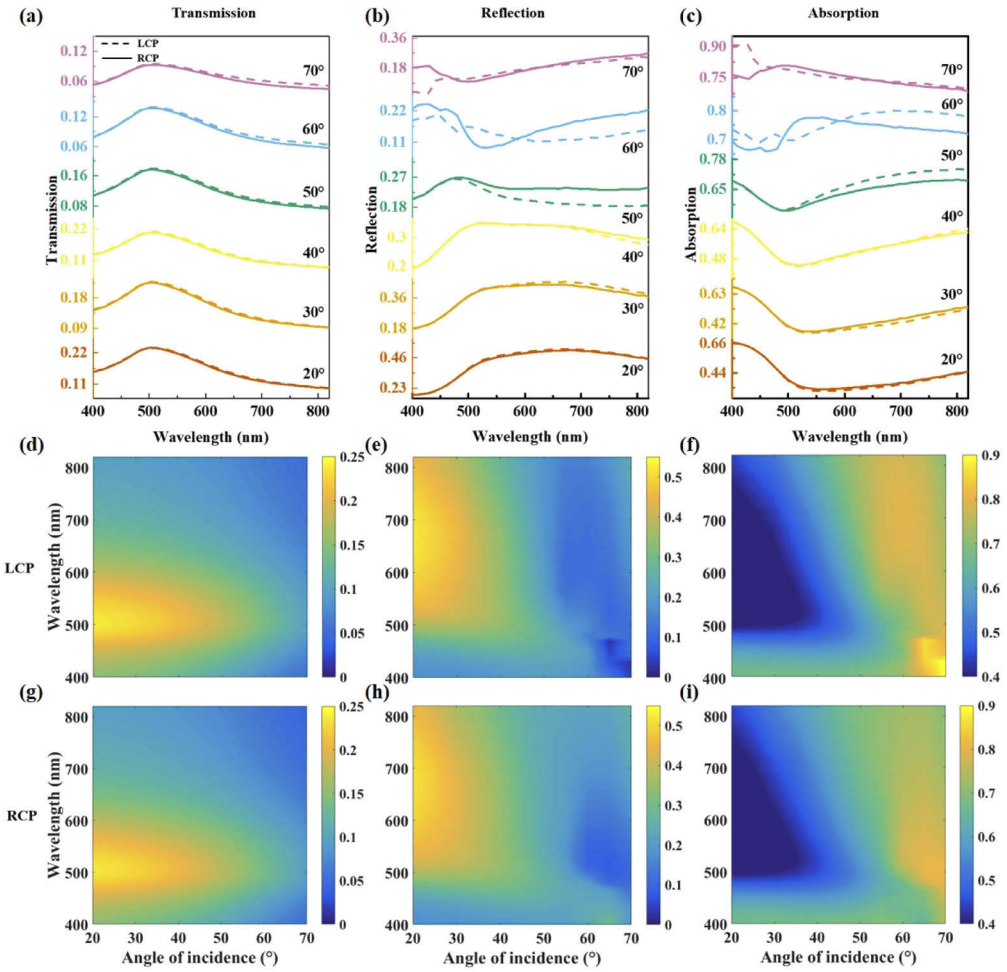

Fig. 4. Optical response under circularly polarized excitation. (a-c) Transmission, reflection and absorption spectra of the sample at different angles of incidence of left and right circularly polarized (LCP and RCP) light. (d-f) Contour mappings of LCP light, corresponding to a-c. (g-i) Contour mappings of RCP light, corresponding to a-c.

In the case of transmittance [Figs. 4(a), 4(d), and 4(g)], the difference between LCP and RCP in the 400-820 nm range is small at all incident angles, resulting in a low circular dichroism (CD) signal, which is on the order of 10^{-3} [Figs. 5(a) and 5(d)]. According to the transmission, reflection, and absorption spectra shown in Figs. 4(a)–4(i), the absorption difference is mainly attributed to the circular dichroic response of reflection rather than transmission. However, compared to the absorption CD i.e., a maximum CD of 0.044 at 520 nm at AOI = 60° in Figs. 5(c) and 5(f)]', the reflection CD is about one order of magnitude greater.

Furthermore, when a wave with initially linear polarization propagates through an optically active and anisotropic medium, it becomes elliptically polarized. The output polarization ellipse is presented to show the tunable polarization conversion through varying the incident angle and wavelength when illuminated by linearly polarized light, as depicted in Fig. 6. The ellipticity angle η is defined such that $\tan(\eta)$ is equal to the ratio of the minor and major axes of the ellipse. For the case of reflection [Figs. 6(a)–6(h)], the converted polarization states at short wavelengths (e.g., $\lambda = 450$ nm) are very close to the linear polarization states, with the ellipticity angle η in

Optics EXPRESS

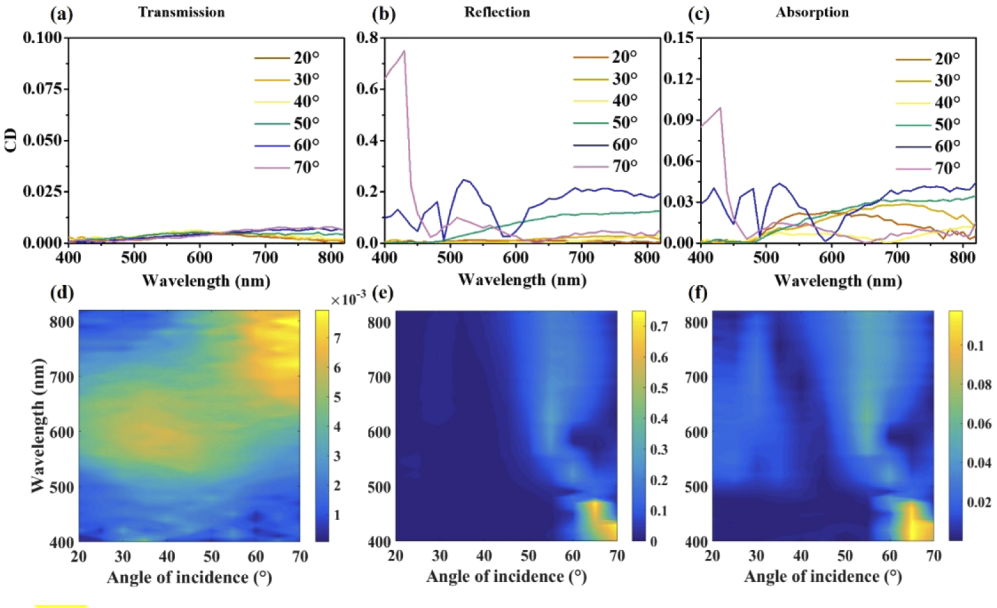

Fig. 5. Circular dichroism response. (a-c) Transmission, reflection, and absorption CD spectra of the sample at different angles of incidence. (d-f) Contour mappings of CD spectra corresponding to a-c.

the range of 0-3°. As the wavelength is increased beyond 500 nm, we observe that the output states are elliptically polarized farther from linearly polarized states at large incident angles (AOI = 50-70°). For instance, at a wavelength of 750 nm with an incident angle of 60°, the ellipticity angle reaches a maximum of 10° under s-polarized excitation. On the other hand, for the case of transmission [Figs. 6(i)–6(p)], we observe that the converted polarization states could also be modulated by both the incident angle and azimuthal rotation of the incident linearly polarized light, resulting in an output ellipticity range of 0-5° under p-polarized excitation, and 0-7° under s-polarized excitation. The underlying reason behind this is discussed in the Appendix Note A6 and Figs. 11(a)–11(f).

The circular dichroism effect from our sample may seem counterintuitive, because it is routinely observed in media lacking mirror symmetry, namely chiral materials [27]. However, a strong chiroptical response is observed in our intrinsically non-chiral anisotropic metamaterials by implementing a large oblique incidence. The reason behind this is that, in such a system, the non-chiral structure together with the incident waves form a geometrical arrangement that cannot be superimposed with its mirror image, and thus the whole arrangement is chiral. Specifically, the wave vector **k**, the vector normal to the sample surface **n**, and the direction of the symmetry axis of the metamaterial unit cell **b** [i.e., the direction of the short axis b in Fig. 2(d)] form a chiral triad, giving rise to the chiroptical effect. This mechanism of extrinsic chirality was first identified in nematic liquid crystals [52,53], and later in artificial planar structures [25,26,54–56]. On the other hand, from the electrodynamic point of view, similarly to how it happens in conventional 3D-chiral media, the observed optical activity effect results from the simultaneous presence of electric and magnetic responses in the structure [57,58]. At normal or small oblique incidence, the induced electric dipole and magnetic dipole moments oscillate along strictly (or nearly) perpendicular directions, and no (or almost no) optical activity is observed. At large oblique incidence (AOI = 50-70°), the main axes of the induced electric and magnetic moments are no longer perpendicular, resulting in a non-zero projection of the induced magnetic dipole on the

Optics EXPRESS

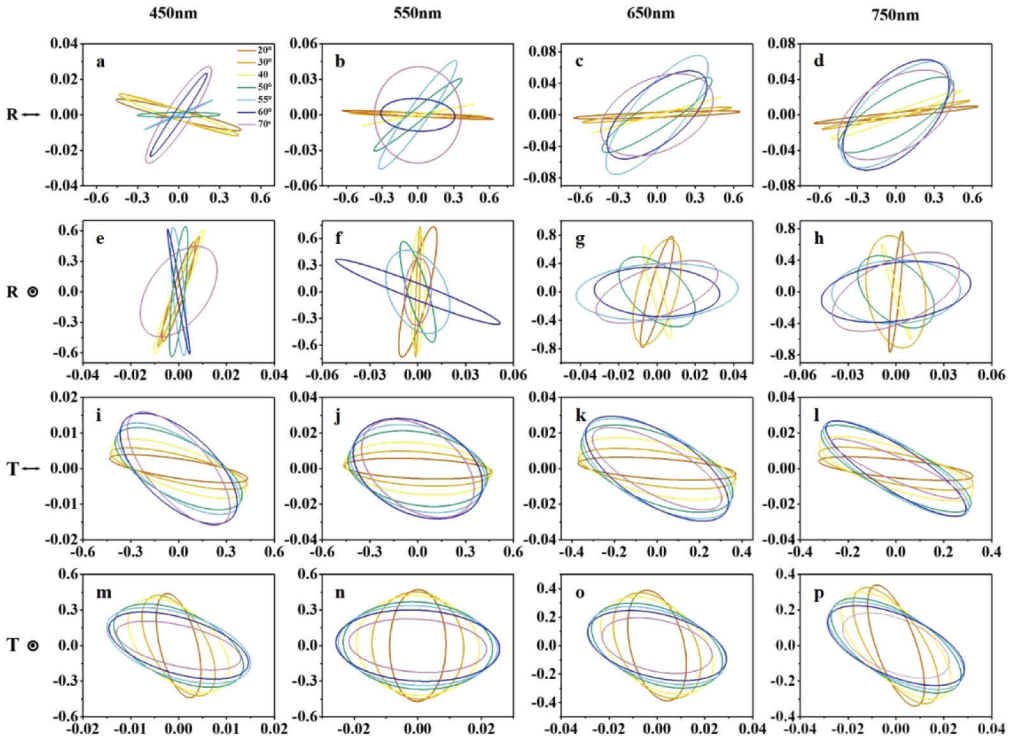

Fig. 6. Polarization state of the light output. (a-d) Polarization-state ellipses for the reflected light when the input wave is a p-polarized light, at wavelengths of 450 nm, 550 nm, 650 nm and 750 nm, respectively. (e-h) Polarization-state ellipses for the reflected light when the input wave is s-polarized light, corresponding to a-d. (i-l) Polarization-state ellipses for the transmitted light when the input wave is p-polarized light, corresponding to a-d. (m-p) Polarization-state ellipses for the transmitted light when the input wave is s-polarized light, corresponding to a-d.

induced electric dipole, which are the right conditions for the metamaterials to scatter with a polarization change. This polarization is optical activity, which can also be termed extrinsic chirality, owing to the non-chiral nature of the studied structures.

3. Conclusion

We demonstrate a simple and convenient nanofabrication strategy to successfully obtain anisotropic metamaterials by glancing angle deposition into AAO templates. Our approach can be readily extended to many materials including metals, dielectrics, semiconductors and organic materials that are capable of fabrication by physical vapor deposition. And we present experimental, analytical and simulated results, showing that a novel non-chiral meta-device can produce giant circular dichroism at oblique incident angles in the visible and near infrared range. Furthermore, the output polarization ellipse could be finely tuned with varying the angle of incident linearly polarized light. Owing to the large circular dichroism and tunability of the polarization response, combined with the capability of large-scale and cost-effective fabrication, such meta-device can be used for chiral bio-sensing, polarization converters, catalysis and so on.

Optics EXPRESS

Appendix

A1. Numerical simulations of the far-field optical response

To verify our experimental results, we have conducted the finite difference time domain (FDTD) simulations. The unit cell is shown in Fig. 1(c), and has t_1=33 ± 5 nm, t_2=178 ± 10 nm, a=70 ± 10 nm, and b=42 ± 10 nm. The Bloch boundary condition is used on four sides, and a perfectly matched layer is used on the top and at the bottom. At normal incidence, we calculate the transmittance under x- and y- direction polarized excitation, respectively. The simulation results are similar to the experiment. In particular, along the plasmonic resonance modes at around 500 nm, the behaviors in Fig. 7(b) are comparable with those in Fig. 7(a). Although the major features observed from the experiment are consistent with the simulations, discrepancies are also present. These discrepancies arise from the fact that applying the simplified unit cell, as shown in Fig. 1(c), usually underestimates the fine details of the system, such as surface roughness and irregular shape non-uniformity, that are necessary for reproducing simulated results that perfectly align with the experiment. Therefore, numerical simulation serves as a tool to check the trustworthiness of our measurements.

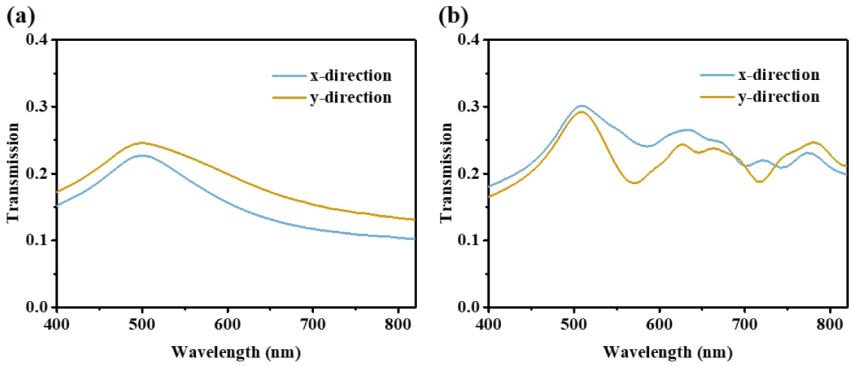

Fig. 7. (a) Experimentally measured transmittance under x- and y- polarized excitation at normal incidence. (b) Numerically simulated transmittance under x- and y- polarized excitation at normal incidence.

A2. Numerical simulations of the near-field distributions

To reveal the physical origin of the spectral feature of the proposed meta-devices, the electric field distribution is analyzed using FDTD simulations. Figures 8(a)–8(h) show the electric field distribution for the nanocone array under a 20° incident angle for p- (x-direction) and s- (y-direction) polarizations. At the shorter wavelength (λ = 500 nm), which is the plasmonic resonant wavelength, the fields are contained in the air cavity, whereas at the longer wavelength (λ = 700 nm), which is far from the plasmonic resonance, the air cavity is screened and the fields are concentrated outside of the air cavity. Figures 8(i)–8(p) show the electric field distribution for the nanocones under a 60° incident angle. At the shorter wavelength (λ = 500 nm), the enhanced fields are around the bottom edge of the Au nanocone. Meanwhile, due to the symmetry breaking, we observed that the fields are concentrated outside of the air cavity for p-polarization, but inside for the s-polarization. Thus, we might expect a larger deviation between p- and s-polarized transmission. At the longer wavelength (λ = 700 nm), the deviation of the electric field between p- and s- polarization follows a similar trend, except that the enhanced fields are concentrated not at the bottom but at the top edge of the Au nanocone under p-polarization, resulting in a larger deviation between p- and s-polarized transmission compared to that of the small angle of incidence (20°), which can be seen in Fig. 3(a).

Optics EXPRESS

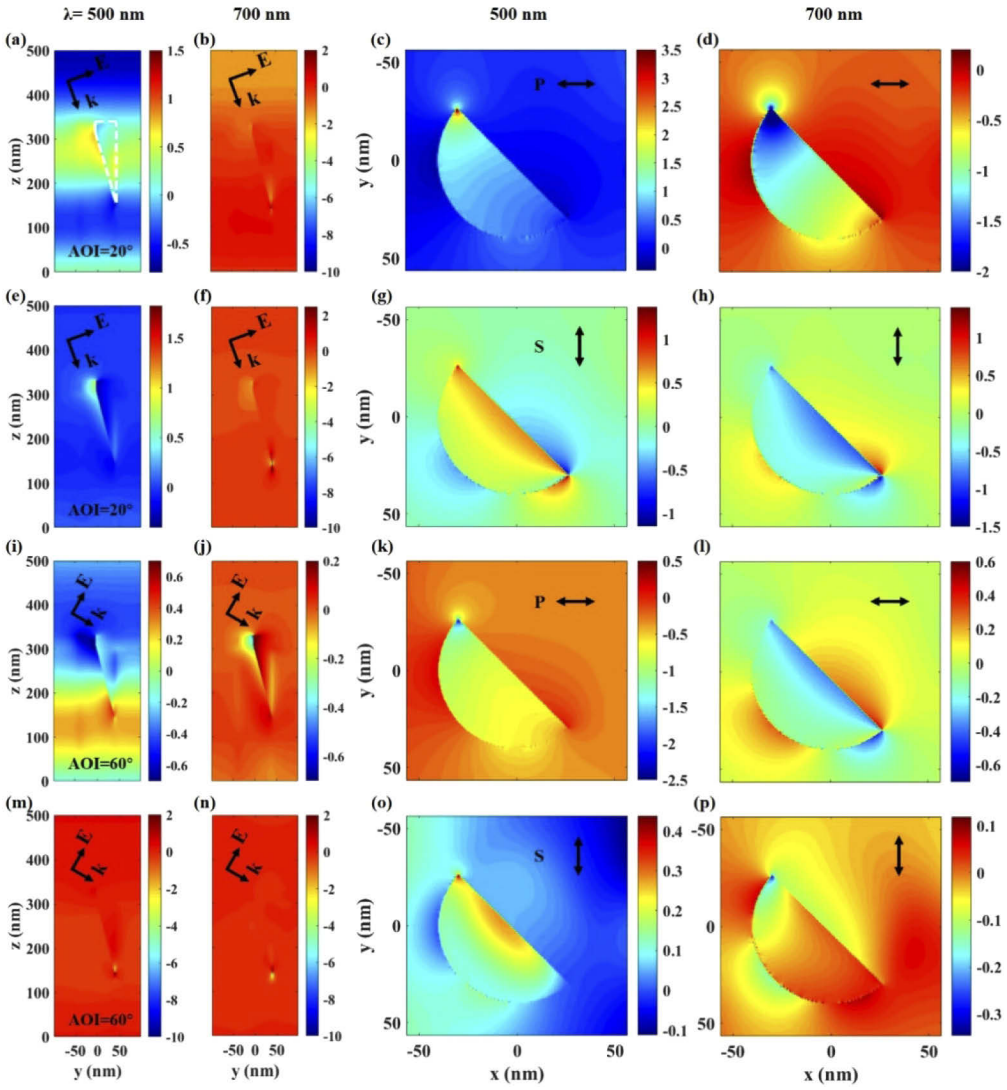

Fig. 8. (a-d) Simulated near-field map of the x-component of the electric field (Ex) for the metamaterial plasmonic mode excited by p-polarized light, with an angle of incidence of 20°. (e-h) Simulated near-field map of the Ex for the metamaterial plasmonic mode excited by s-polarized light, with an angle of incidence of 20°. (i-l) Simulated near-field map of the Ex for the metamaterial plasmonic mode excited by p-polarized light, with an angle of incidence of 60°. (m-p) Simulated near-field map of the Ex for the metamaterial plasmonic mode excited by s-polarized light, with an angle of incidence of 60°. The 1st and 2nd columns are in the plane x = 0, at wavelengths of 500 nm and 700 nm, respectively. The 3rd and 4th columns are in the plane z = 315 nm (referred to the bottom of the nanohole, defined as z = 0), at wavelengths of 500 nm and 700 nm, respectively.

A3. Derivations of the Jones matrix, and calculations of linearly polarized transmission and reflection

The ellipsometric parameters are directly related to the Fresnel reflection coefficients for the linear polarization states, according to

$$\tan(\Psi) \cdot e^{i\Delta} = \frac{r_{pp}}{r_{ss}}. \tag{3a}$$

Optics EXPRESS

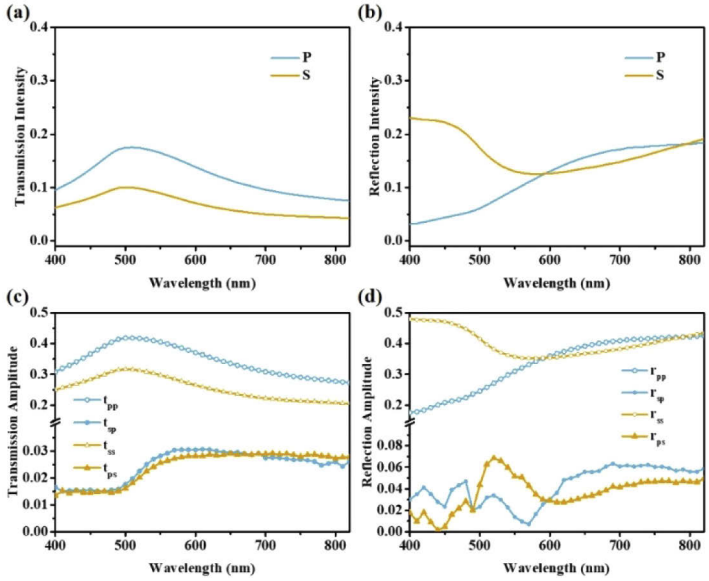

Fig. 9. (a) Experimentally measured transmittance under p- and s- polarized excitation. (b) Experimentally measured reflectance under p- and s- polarized excitation. (c) Calculated co- and cross- linearly polarized transmission amplitude. (d) Calculated co- and cross- linearly polarized reflection amplitude. The angle of incidence is 60°.

$$\tan(\Psi_{ps}) \cdot e^{i\Delta_{ps}} = \frac{r_{ps}}{r_{pp}}. \tag{3b}$$

$$\tan(\Psi_{sp}) \cdot e^{i\Delta_{sp}} = \frac{r_{sp}}{r_{ss}}. \tag{3c}$$

Together with the relation of

$$|r_p|^2 = |r_{pp}|^2 + |r_{sp}|^2. \tag{3d}$$

where $|r_p|^2$ is the measured reflection under p-polarized light incidence, the subscript ps represents the p-polarized reflected electric field component in response to s-polarized incident electric field, and vice versa for sp, one can obtain the full reflection coefficients, that is, R_{pp}, R_{ps}, R_{sp}, and R_{ss}, of the complex Jones matrix R for linearly polarized light as

$$\begin{pmatrix} R_{pp} & R_{ps} \\ R_{sp} & R_{ss} \end{pmatrix} = \begin{pmatrix} r_{pp}e^{i\theta_{pp}} & r_{ps}e^{i\theta_{ps}} \\ r_{sp}e^{i\theta_{sp}} & r_{ss}e^{i\theta_{ss}} \end{pmatrix}. \tag{4}$$

Optics EXPRESS

A4. Calculations of circularly polarized transmission and reflection

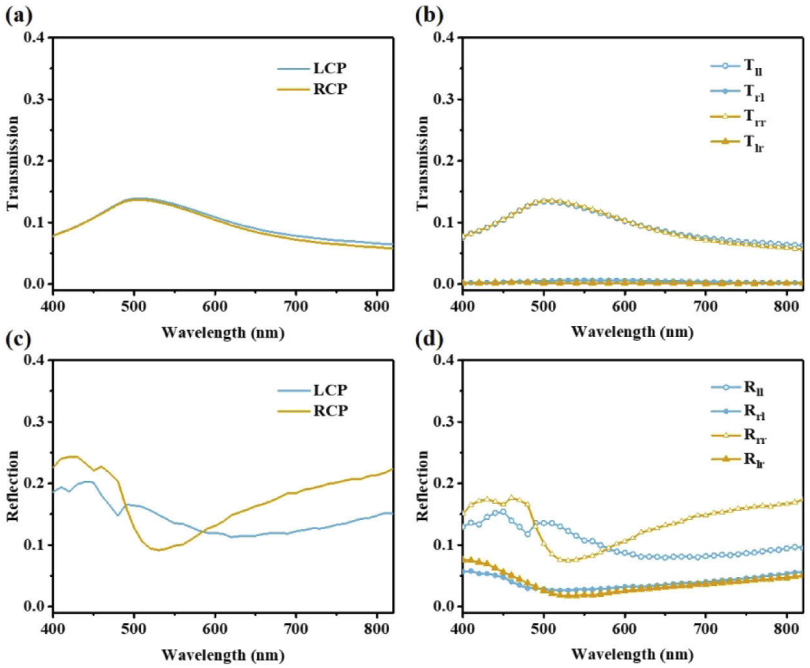

Fig. 10. (a) Calculated transmittance under left-handed circularly polarized (LCP) light excitation and right-handed circularly polarized (RCP) light excitation. (b) Calculated co- and cross- circularly polarized transmittance. (c) Calculated reflectance under LCP and RCP light excitation. (d) Calculated co- and cross- circularly polarized reflectance. The angle of incidence is 60°.

A5. Incident angle and wavelength dependent ellipticity

It is known that for moderate changes, the ellipticity of the output wave will contain contributions from circular dichroism (CD) and linear birefringence (LB) [58]. Meanwhile, CD is proportional to the degree of circular polarization (DoCP), and DoCP is defined as $\theta = (E_{RCP} - E_{LCP})/(E_{RCP} + E_{LCP})$, where E_{RCP} and E_{LCP}. are the magnitudes of the electric field vectors of the right- and left- circularly polarized light, respectively. From Figs. 11(a), 11(c) and 11€, we can conclude that CD is the dominant contribution to the ellipticity change in the reflection geometry; for instance, at a wavelength of 750 nm and an incident angle of 60°, the CD contributes 88% to the total ellipticity under p-polarized excitation, and 65% to the total ellipticity under s-polarized excitation. On the other hand, for the case of transmission [Figs. 5(i)–5(p) in the main text], we observe that the converted polarization states could also be modulated by both the incident angle and azimuthal rotation of the incident linearly polarized light, resulting in an output ellipticity range of 0-5° under p-polarized excitation, and 0-7° under s-polarized excitation. However, in contrast to the reflection, linear birefringence (LB) dominates the contribution to the ellipticity angle η, while circular dichroism (CD) makes a negligible contribution, as presented in Figs. 11(b), 11(d) and 11(f).

Optics EXPRESS

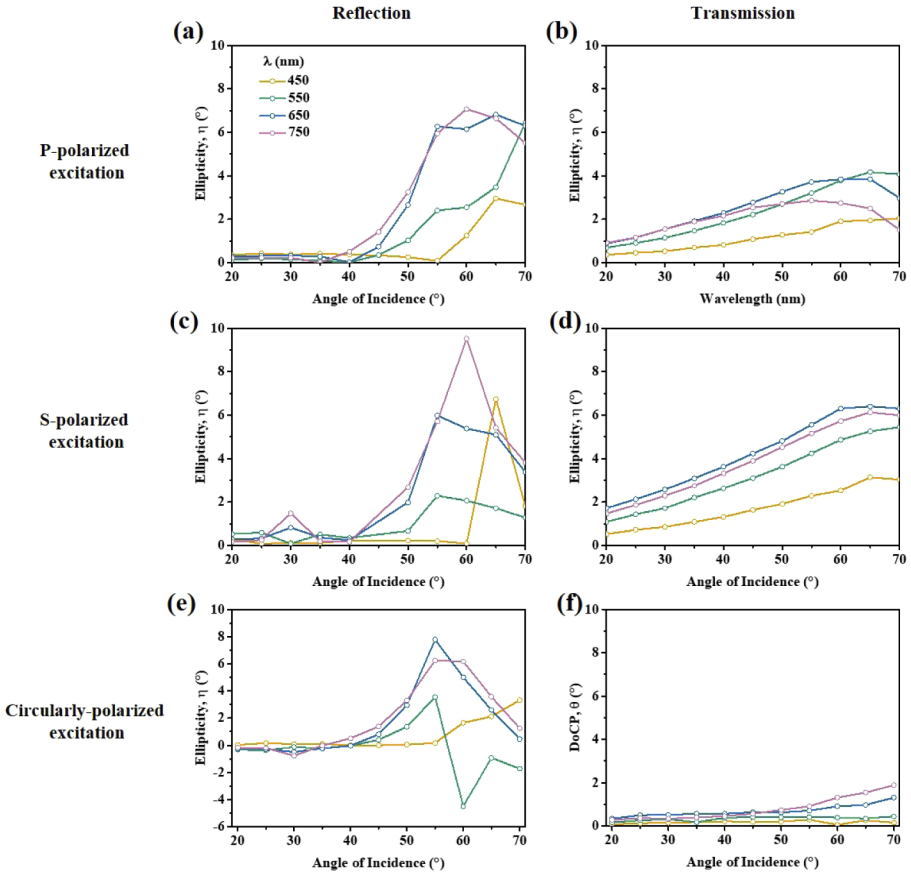

Fig. 11. Incident angle dependent ellipticity for reflection and transmission at different wavelengths of 450 nm, 550 nm, 650 nm and 750 nm, under p-polarized excitation (a-b), s-polarized excitation (c-d). Incident angle dependent degree of circular polarization (DoCP) for reflection and transmission, respectively (e-f).

Funding

Beijing Municipal Commission of Education (BJJWZYJH01201910007022); National Natural Science Foundation of China (61775019).

Acknowledgments

Y. F. acknowledges the support of the bridge scholarship by the Equal Opportunity Council of the University of Konstanz. C. A. N acknowledges the Brown Family Internship Grant. The authors thank Qunshuo Wei and Shuangqi Zhu for valuable discussions.

Disclosures

The authors declare no conflicts of interest.

References

1. N. Yu, P. Genevet, M. A. Kats, F. Aieta, J. P. Tetienne, F. Capasso, and Z. Gaburro, "Light propagation with phase discontinuities: generalized laws of reflection and refraction," Science **334**(6054), 333–337 (2011).

Optics EXPRESS

2. L. H. Nicholls, F. J. Rodríguez-Fortuño, M. E. Nasir, R. M. Córdova-Castro, N. Olivier, G. A. Wurtz, and A. V. Zayats, "Ultrafast synthesis and switching of light polarization in nonlinear anisotropic metamaterials," Nat. Photonics **11**(10), 628–633 (2017).
3. L. Quan, J. Kang, C. Ning, and P. Yang, "Nanowires for photonics," Chem. Rev. **119**(15), 9153–9169 (2019).
4. J. Zhu, Z. Wang, S. Lin, S. Jiang, X. Liu, and S. Guo, "Low-cost flexible plasmonic nanobump metasurfaces for label-Free sensing of serum tumor marker," Biosens. Bioelectron. **150**, 111905 (2020).
5. A. V. Kabashin, P. Evans, S. Pastkovsky, W. Hendren, G. A. Wurtz, R. Atkinson, R. Pollard, V. A. Podolskiy, and A. V. Zayats, "Plasmonic nanorod metamaterials for biosensing," Nat. Mater. **8**(11), 867–871 (2009).
6. W. T. Chen, A. Y. Zhu, V. Sanjeev, M. Khorasaninejad, Z. Shi, E. Lee, and F. Capasso, "A broadband achromatic metalens for focusing and imaging in the visible," Nat. Nanotechnol. **13**(3), 220–226 (2018).
7. N. A. Rubin, G. D'Aversa, P. Chevalier, Z. Shi, W. T. Chen, and F. Capasso, "Matrix Fourier optics enables a compact full-Stokes polarization camera," Science **365**(6448), eaax1839 (2019).
8. H. M. Luong, M. T. Pham, B. Ai, T. D. Nguyen, and Y. Zhao, "Magnetoplasmonic properties of Ag-Co composite nanohole arrays," Phys. Rev. B **99**(22), 224413 (2019).
9. G. Armelles, A. Cebollada, A. Garcia-Martin, and M. U. González, "Magnetoplasmonics: combining magnetic and plasmonic functionalities," Adv. Opt. Mater. **1**(1), 10–35 (2013).
10. Z. Lin, L. Huang, Z. T. Xu, X. Li, T. Zentgraf, and Y. Wang, "Four-wave mixing holographic multiplexing based on nonlinear metasurfaces," Adv. Opt. Mater. **7**(21), 1900782 (2019).
11. R. Zhao, B. Sain, Q. Wei, C. Tang, X. Li, T. Weiss, L. Huang, Y. Wang, and T. Zentgraf, "Multichannel vectorial holographic display and encryption," Light: Sci. Appl. **7**(1), 95 (2018).
12. Q. Wei, B. Sain, Y. Wang, B. Reineke, X. Li, L. Huang, and T. Zentgraf, "Simultaneous spectral and spatial modulation for color printing and holography using all-dielectric metasurfaces," Nano Lett. **19**(12), 8964–8971 (2019).
13. Z. Xu, L. Huang, X. Li, C. Tang, Q. Wei, and Y. Wang, "Quantitatively correlated amplitude holography based on photon sieves," Adv. Opt. Mater. **8**(2), 1901169 (2020).
14. X. Ni, Z. J. Wong, M. Mrejen, Y. Wang, and X. Zhang, "An ultrathin invisibility skin cloak for visible light," Science **349**(6254), 1310–1314 (2015).
15. Y. Huang, M. Pu, F. Zhang, J. Luo, X. Li, X. Ma, and X. Luo, "Broadband functional metasurfaces: achieving nonlinear phase generation toward achromatic surface cloaking and lensing," Adv. Opt. Mater. **7**(7), 1801480 (2019).
16. Y. Feng, P. Kim, C. A. Nemitz, K. D. Kim, Y. Park, K. Leo, J. Dorman, J. Weickert, Y. Wang, and L. Schmidt-Mende, "Boosting charge collection efficiency via large-area free-standing Ag/ZnO core-shell nanowire array electrodes," Prog. Nat. Sci. **29**(2), 124–128 (2019).
17. P. Yu, L. V. Besteiro, Y. Huang, J. Wu, L. Fu, H. H. Tan, C. Jagadish, G. P. Wiederrecht, A. O. Govorov, and Z. Wang, "Broadband metamaterial absorbers," Adv. Opt. Mater. **7**(3), 1800995 (2019).
18. E. Arbabi, S. M. Kamali, A. Arbabi, and A. Faraon, "Vectorial holograms with a dielectric metasurface: ultimate polarization pattern generation," ACS Photonics **6**(11), 2712–2718 (2019).
19. M. J. P. Balthasar, N. A. Rubin, R. C. Devlin, B. Groever, and F. Capasso, "Metasurface polarization optics: independent phase control of arbitrary orthogonal states of polarization," Phys. Rev. Lett. **118**(11), 113901 (2017).
20. J. K. Gansel, M. Thiel, M. S. Rill, M. Decker, K. Bade, V. Saile, G. von Freymann, S. Linden, and M. Wegener, "Gold helix photonic metamaterial as broadband circular polarizer," Science **325**(5947), 1513–1515 (2009).
21. N. Passilly, K. Ventola, P. Karvinen, P. Laakkonen, J. Turunen, and J. Tervo, "Polarization conversion in conical diffraction by metallic and dielectric subwavelength gratings," Appl. Opt. **46**(20), 4258–4265 (2007).
22. V. G. Kravets, A. V. Kabashin, W. L. Barnes, and A. N. Grigorenko, "Plasmonic surface lattice resonances: a review of properties and applications," Chem. Rev. **118**(12), 5912–5951 (2018).
23. B. M. Maoz, A. B. Moshe, D. Vestler, O. Bar-Elli, and G. Markovich, "Chiroptical effects in planar achiral plasmonic oriented nanohole arrays," Nano Lett. **12**(5), 2357–2361 (2012).
24. N. Zhou, Y. Bekenstein, C. N. Eisler, D. Zhang, A. M. Schwartzberg, P. Yang, A. P. Alivisatos, and J. A. Lewis, "Perovskite nanowire-block copolymer composites with digitally programmable polarization anisotropy," Sci. Adv. **5**(5), eaav8141 (2019).
25. T. Cao, C. Wei, and Y. Li, "Dual-band strong extrinsic 2D chirality in a highly symmetric metal-dielectric-metal achiral metasurface," Opt. Mater. Express **6**(2), 303–311 (2016).
26. T. Cao, C. Wei, and L. Mao, "Numerical study of achiral phase change metamaterials for ultrafast tuning of giant circular conversion dichroism," Sci. Rep. **5**(1), 14666 (2015).
27. J. Bao, N. Liu, H. Tian, Q. Wang, T. Cui, W. Jiang, S. Zhang, and T. Cao, "Chirality Enhancement Using Fabry–Pérot-Like Cavity," Research (Washington, DC, U. S.) **2020**, 1–9 (2020).
28. S. Li, L. Xu, W. Ma, X. Wu, M. Sun, H. Kuang, L. Wang, N. A. Kotov, and C. Xu, "Dual-mode ultrasensitive quantification of microRNA in living cells by chiroplasmonic nanopyramids self-assembled from gold and up-conversion nanoparticles," J. Am. Chem. Soc. **138**(1), 306–312 (2016).
29. X. T. Kong, L. V. Besteiro, Z. Wang, and A. O. Govorov, "Plasmonic chirality and circular dichroism in bioassembled and nonbiological systems: theoretical background and recent progress," Adv. Mater. 1801790 (2018).
30. M. J. Urban, C. Zhou, X. Duan, and N. Liu, "Optically resolving the dynamic walking of a plasmonic walker couple," Nano Lett. **15**(12), 8392–8396 (2015).
31. J. Pendry, "A chiral route to negative refraction," Science **306**(5700), 1353–1355 (2004).

Optics EXPRESS

32. Z. Fan and A. O. Govorov, "Chiral nanocrystals: plasmonic spectra and circular dichroism," Nano Lett. **12**(6), 3283–3289 (2012).
33. Z. Liu, Y. Xu, C. Y. Ji, S. Chen, X. Li, X. Zhang, Y. Yao, and J. Li, "Fano-enhanced circular dichroism in deformable stereo metasurfaces," Adv. Mater. **32**(8), 1907077 (2020).
34. B. Bai, Y. Svirko, J. Turunen, and T. Vallius, "Optical activity in planar chiral metamaterials: theoretical study," Phys. Rev. A **76**(2), 023811 (2007).
35. M. Wang, R. Salut, H. Lu, M. A. Suarez, N. Martin, and T. Grosjean, "Subwavelength polarization optics via individual and coupled helical traveling-wave nanoantennas," Light: Sci. Appl. **8**(1), 76 (2019).
36. A. Nemati, Q. Wang, M. H. Hong, and J. H. Teng, "Tunable and reconfigurable metasurfaces and metadevices," Opto-Electron. Adv. **1**(5), 18000901–18000925 (2018).
37. Y. Li and M. Hong, "Parallel Laser Micro/Nano-Processing for Functional Device Fabrication," Laser Photonics Rev. **14**(3), 1900062 (2020).
38. D. Serien and K. Sugioka, "Fabrication of three-dimensional proteinaceous micro- and nano-structures by femtosecond laser cross-linking," Opto-Electron. Adv. **1**(4), 180008 (2018).
39. Y. Zhao, M. A. Belkin, and A. Alù, "Twisted optical metamaterials for planarized ultrathin broadband circular polarizers," Nat. Commun. **3**(1), 870 (2012).
40. Y. Fang, R. Verre, L. Shao, P. Nordlander, and M. Käll, "Hot electron generation and cathodoluminescence nanoscopy of chiral split ring resonators," Nano Lett. **16**(8), 5183–5190 (2016).
41. F. Keller, M. S. Hunter, and D. L. Robinson, "Structural features of oxide coatings on aluminium," J. Electrochem. Soc. **100**(9), 411 (1953).
42. H. Masuda, "Ordered metal nanohole arrays made by a two-step replication of honeycomb structures of anodic alumina," Science **268**(5216), 1466–1468 (1995).
43. K. Nielsch, J. Choi, K. Schwirn, R. B. Wehrspohn, and U. Gösele, "Self-ordering regimes of porous alumina: the 10 porosity rule," Nano Lett. **2**(7), 677–680 (2002).
44. M. Pérez-Page, E. Yu, J. Li, M. Rahman, D. M. Dryden, R. Vidu, and P. Stroeve, "Template-based syntheses for shape controlled nanostructures," Adv. Colloid. Interfac. **234**, 51–79 (2016).
45. M. Jani, M. Abdul, A. S. Habiballah, B. A. Halim, M. Zikri, A. Zulkifli, F. Wahida, A. H. Mahmud, and H. Yazid, "Nanoporous anodic aluminum oxide (NAAO) for catalytic, biosensing and template synthesis applications," Curr. Nanosci. **15**(1), 49–63 (2018).
46. Y. Feng, D. Kim, C. A. Nemitz, P. Kim, T. Pfadler, M. Gerigk, S. Polarz, J. A. Dorman, J. Weickert, and L. Schmidt-Mende, "Uniform large-area free-standing silver nanowire arrays on transparent conducting substrates," J. Electrochem. Soc. **163**(8), D447–D452 (2016).
47. Q. Wang, E. Plum, Q. Yang, X. Zhang, Q. Xu, Y. Xu, J. Han, and W. Zhang, "Reflective chiral meta-holography: multiplexing holograms for circularly polarized waves," Light: Sci. Appl. **7**(1), 25 (2018).
48. C. Menzel, C. Helgert, C. Rockstuhl, E. B. Kley, A. Tünnermann, T. Pertsch, and F. Lederer, "Asymmetric transmission of linearly polarized light at optical metamaterials," Phys. Rev. Lett. **104**(25), 253902 (2010).
49. B. Yeom, H. Zhang, H. Zhang, J. Park, K. Kim, A. O. Govorov, and N. A. Kotov, "Chiral plasmonic nanostructures on achiral nanopillars," Nano Lett. **13**(11), 5277–5283 (2013).
50. M. Hentschel, M. Schäferling, X. Duan, and N. Liu, "Chiral plasmonics," Science **3**(5), e1602735 (2017).
51. N. H. Cho, G. H. Byun, Y. C. Lim, S. W. Im, H. Kim, H. E. Lee, H. Y. Ahn, and K. T. Nam, "Uniform chiral gap synthesis for high dissymmetry factor in single plasmonic gold nanoparticle," ACS Nano **14**(3), 3595–3602 (2020).
52. R. Williams, "Optical rotatory effect in the nematic liquid phase of p-azoxyanisole," Phys. Rev. Lett. **21**(6), 342–344 (1968).
53. A. D. Buckingham and M. B. Dunn, "Optical activity of oriented molecules," J. Chem. Soc. A. 1988–1991 (1971).
54. P. Lai, G. Dong, W. Wang, T. Chen, T. Lv, B. Lv, Z. Zhu, Y. Li, C. Guan, and J. Shi, "Angle enhanced circular dichroism in bilayer 90°-twisted metamaterial," Opt. Express **28**(10), 15071–15080 (2020).
55. F. Wang, Z. Wang, and J. Shi, "Theoretical study of high-Q Fano resonance and extrinsi chirality in an ultrathin Babinet-inverted metasurface," J. Appl. Phys. **116**(15), 153506 (2014).
56. L. Mao, K. Liu, S. Zhang, and T. Cao, "Extrinsically 2D-chiral metamirror in near-infrared region," ACS Photonics **7**(2), 375–383 (2020).
57. E. Plum, X. X. Liu, V. A. Fedotov, Y. Chen, D. P. Tsai, and N. I. Zheludev, "Optical activity without chirality," Phys. Rev. Lett. **102**(11), 113902 (2009).
58. M. Ren, E. Plum, J. Xu, and N. Zheludev, "Giant nonlinear optical activity in a plasmonic metamaterial," Nat. Commun. **3**(1), 833 (2012).